Integrating Materials and Manufacturing Innovation (2022) 11:327–338
https://doi.org/10.1007/s40192-022-00265-4

TECHNICAL ARTICLE

On the Prediction of Uniaxial Tensile Behavior Beyond the Yield Point of Wrought and Additively Manufactured Ti-6Al-4V

Maria J. Quintana[1,2] · Andrew J. Temple[1,2] · D. Gary Harlow[3] · Peter C. Collins[1,2,4]

Received: 29 March 2022 / Accepted: 25 May 2022 / Published online: 5 July 2022

Abstract

In this paper, phenomenological relationships are presented that permit the prediction of the plastic regime of stress–strain curves using a limited number of parameters. These relationships were obtained from both conventional (wrought + β annealed) and additively manufactured (i.e., "3D printed") Ti-6Al-4V. Three different methods of additive manufacturing have been exploited to produce the materials, including large-volume electron beam additive manufacturing, large-volume laser hot wire additive manufacturing, and small-volume selective laser melting. The general fundamental expressions are independent not only of the additive manufacturing process, but also of a wide variety of post-deposition heat treatments, however the coefficients are specific to material states. Thus, this work demonstrates that it is possible to predict not only the ultimate tensile strength, but also the full true stress, true strain curves, if certain parameters of the material are known. In general, the prediction of ultimate tensile strength are within 5% of the experimentally measured values across all additive manufacturing variants and subsequent heat treatments. The absolute values of ultimate tensile strength range from ~ 910 MPa to ~ 1170 MPa for the single alloy Ti-6Al-4V. Data representing 113 explicit samples are included in this work.

Keywords Titanium · Ti-6Al-4V · Mechanical properties · Ultimate tensile strength · Work hardening · Kocks–Mecking–Estrin model

Introduction

With the rapid growth in advanced materials processing, especially with additive manufacturing (i.e., "3D printing"), it is necessary to develop similarly rapid strategies to qualify the materials that are produced from these processes. Materials qualification invariably seeks to assess with a degree of statistical rigor the materials state and the attending properties and will often relate these properties to a particular material's composition (heat/lot) or the manufacturing process. The product of these assessments are databases, often investigated to give design allowables and/or probability distribution functions of particular properties. However, the cost associated with establishing these databases which underpin the design allowables/probability distribution functions is significant. Thus, it would be most beneficial and economically advantageous if it were possible to establish the process-property relationships of an alloy X processed using any of a number of possible methods (Y_i). In pursuing this objective, to the extent possible, it should be recognized that the "materials state" governs the properties [1–3].

In previous work, such property predictions have been developed for yield strength [4]. Yield strength for Ti-6Al-4V was found to be strongly governed by the average materials state, especially composition, dislocation density, and texture, though for other alloys variables such as grain size and phase fraction, among others, should be considered. However, yield strength is not the only important engineering property for which such predictions need to be established. Other properties, including additional uniaxial tensile test metrics (such as the ultimate tensile strength

Maria J. Quintana and Andrew J. Temple contributed equally.

✉ Peter C. Collins
pcollins@iastate.edu

[1] Department of Materials Science and Engineering, Iowa State University, Ames, IA 50011, USA

[2] Center for Advanced Nonferrous Structural Alloys, A Joint NSF I/UCRC Between Iowa State University and the Colorado School of Mines, Golden, CO 80401, USA

[3] Department of Mechanical Engineering and Mechanics, Lehigh University, Bethlehem, PA 18015, USA

[4] Ames Laboratory, Ames, IA 50011, USA

and elongation) are important. While the need to establish these other property models could be perceived as simply an exercise to establish "just one more" process-property relationship, they are notably different from the prior work in two distinct ways. Firstly, they include as a variable an external stimuli (i.e., the strain) that dynamically changes as a quantifiable aspect of the materials state. Thus, while our work was initially motivated to predict the ultimate tensile strength (a discrete property representing a single point on a stress–strain curve), it became clear that it was not only possible, but useful to predict the stress–strain curve up to the ultimate tensile strength. Secondly, it is useful to revisit the classical theories which describe the physical processes associated with these other properties.

This paper consists of two equally important aspects. The first is a revisiting of the classical theories of other properties (specifically ultimate tensile strength) and the second is the demonstration of the applicability of these theories to one alloy obtained by a wide variety of additively manufactured processes. The results presented herein may be relevant to those with different perspectives, equally relevant to the practicing AM scientist/engineer where materials state and design allowables are critical and to the study of the fundamentals of mechanical behavior.

When referring to the strength of an engineering material, the yield strength is often cited for design purposes, as it represents the stress at which noticeable plastic deformation begins and is usually the stress value designers and engineers use to set safety factors. Uniaxial tensile tests can be used to measure not only yield strength, but also the ultimate tensile strength, or simply tensile strength, which is the maximum stress that can be sustained by a material prior to strain localization, the onset of necking, and imminent failure. When considering only these two tensile properties (yield strength and ultimate tensile strength) for design purposes, it is easy to forget that plasticity is a path-dependent process that depends enormously on the materials state. Digital records contain a large amount of supplementary information that can be extracted from a simple stress–strain curve, provided that the tools for their interpretation are widely understood. Only using two discrete points, yield strength and ultimate tensile strength, to represent the progression of the tensile response of the material through the elastic and plastic regions up until the onset of necking when there is an entire stress–strain curve with a continuum of stress and strain values creates opportunity for a more comprehensive approach to materials engineering.

Although tensile properties may provide sufficient information in most cases [5], the strain hardenability can provide a more in-depth understanding of the stress–strain behavior and the mechanisms involved, during plastic deformation. Ludwik, Hollomon, Voce, and Swift have developed various empirical equations to describe the stress–strain behavior for a variety of materials [6–9]. A major limitation of these classical models is the geometric nature of fitting to the experimental stress–strain curve. The difficulty of applying these models is the fact that the stress–strain behavior described by these equations is not easily generalizable to samples of the same material condition or manufacturing process. Additionally, a clear connection between the fitting parameters of these equations and the underlying material state does not exist. For example, the measured yield strength and ultimate tensile strength could be nearly identical for two samples with quantifiably different "material states", owing to the competition between different strengthening mechanisms; however, the behavior (i.e., shape) of the stress–strain curve between these discrete points would not necessarily be the same. Therefore, yield strength and ultimate tensile strength alone are insufficient descriptors to capture the details of the plastic behavior observed during a uniaxial tensile test. To understand the strain hardening behavior, it is necessary to elucidate and to quantitatively capture the governing mechanisms that are related to the materials state.

As reported by Hayes et al. [4], the yield strength for Ti-6Al-4V can be calculated by:

$$\begin{aligned}\sigma_{ys} =& 89F_{\mathrm{V}}^{\alpha} + 45F_{\mathrm{V}}^{\beta} + F_{\mathrm{V}}^{\alpha}\left(149x_{\mathrm{Al}}^{0.667} + 759x_{\mathrm{O}}^{0.667}\right) \\ &+ F_{\mathrm{V}}^{\beta}\left(\left(22x_{\mathrm{V}}^{0.7}\right)^{0.5} + \left(235x_{\mathrm{Fe}}^{0.7}\right)^{0.5}\right)^{2} + 150F_{\mathrm{V}}^{\mathrm{col}}\left(t_{\alpha-\mathrm{lath}}\right)^{-0.5}\left(t_{\beta-\mathrm{rib}}\right)^{0.5} \\ &+ 125F_{\mathrm{V}}^{\mathrm{col}}\left(t_{\mathrm{colony}}\right)^{-0.5} + (-1)\mathrm{AxisDebit} + F_{V}^{BW}\alpha \mathrm{GMb}\sqrt{\rho}\end{aligned} \quad (1)$$

where F_{V} are volume fractions of the designated phases/microstructures, x_{M} are the concentrations of each element M (i.e., Al, O, Fe, V), t_{feature} is the thickness of a feature (i.e., the α-laths, β-ribs, and colony scale factor), α is a prefactor term, G is the shear modulus of the material, M is the Taylor factor, b is the Burgers vector, and ρ is the dislocation density. Previously, Eq. 1 has been shown to apply well to both wrought and additively manufactured Ti-6Al-4V. It should be noted that this equation was developed and based upon extensive research into the parameters that do, as well as the parameters that do not, influence yield strength. The details are found elsewhere in the literature.

Although a phenomenological equation to predict yield strength for Ti-6Al-4V has already been developed [4, 10, 11], the dynamic nature of dislocation evolution that governs plastic deformation adds a degree of difficulty to the prediction of mechanical properties beyond the yield point. The evolution of dislocation content is strongly correlated with the evolution of strain (plastic deformation) that is induced during the uniaxial tensile test, and which is then introduced into the material. Unlike the yield strength equation for Ti-6Al-4V, which is composed of "static" variables like composition, phase

fraction, lath thickness, and stored dislocation density to describe the *onset* of permanent plastic deformation, the prediction of ultimate tensile strength relies on "dynamic" variables (e.g., the evolution of dislocation density with changing strain, including not only the creation of dislocations over time, but also their annihilation) [4, 12–15]. One phenomenological model that does account for the evolution of dislocation density is the one proposed by Kocks and Mecking in 1981 [16]. In their work, Kocks–Mecking (KM) proposed a model [17] (Eq. 2) that consists of separate components which describe how the dislocation density changes with changes in strain:

$$\frac{\mathrm{d}\rho}{\mathrm{d}\gamma} = k_1\sqrt{\rho} - k_2\rho \tag{2}$$

where ρ is the dislocation density, γ is the shear strain, k_1 is a constant that considers the dislocation storage of gliding dislocations at the dislocation forest obstacles or dislocation cell walls and k_2 is a strain-rate and temperature-dependent constant associated with the reduction in dislocation density due to annihilation, i.e., dynamic recovery.

Yasnikov, Vinogradov, and Estrin [18–22] continued the development of the model, now known as Kocks–Mecking–Estrin (KME) model, and published the next breakthrough in their explicit solution of Eq. (2), which is obtained after substitution and integration, and translating shear strain to uniaxial tensile strain:

$$\sigma = \sigma_0 + \frac{\alpha \mathrm{GMb}k_1}{k_2}\left(1 - \exp\left(-\frac{k_2 M\varepsilon}{2}\right)\right) \tag{3}$$

where σ_0 is the flow stress of the material excluding strain effects (i.e., the yield strength), α is a prefactor term, G is the shear modulus of the material, M is the Taylor factor, b is the Burgers vector and ε is the plastic strain. In this work, the flow stress is assumed to be the yield stress (σ_{ys}) as measured from a uniaxial tensile test, and the two terms may be used interchangeably. The variable σ_0 will be used when referring to the flow stress/yield stress in equations, tables, and figures hereafter.

As noted previously, one of the most important discrete values that can be extracted from the stress–strain curve is the ultimate tensile strength value. The ultimate tensile stress occurs when the stress creates local non-uniform deformation, and the tensile coupons start forming a neck. The strain when ultimate tensile strength occurs is known as the necking strain.[1] The plastic component of this necking strain $\left(\varepsilon_{n-KME}\right)$ can be obtained using the expanded KME model [18–22], using the same variables:

$$\varepsilon_{n-\mathrm{KME}} = \frac{2}{k_2 M}\ln\left(\frac{\left(2+k_2 M\right)\left(\alpha \mathrm{GbM}k_1\right)}{2\left(\alpha \mathrm{GbM}k_1 + k_2\sigma_0\right)}\right) \tag{4}$$

The KME model has been applied to obtain average coefficients for different manufacturing processes and heat treatment (wrought and additively manufactured Ti-6Al-4V), which can later be used for the prediction of the ultimate tensile strength for individual specimens. Equally importantly, accurate predictions have been made for Ti-6Al-4V produced via three different additive manufacturing processes: electron beam additive manufacturing (EBAM), selective laser melting (SLM) and laser hot wire additive manufacturing (LHW). The ability to compare and analyze results from three independent sources provides a unique opportunity to develop an understanding of the stress–strain behavior for additively manufactured Ti-6Al-4V, as an extension of the previous work on yield strength.

Experimental Procedure

Ti-6Al-4V samples manufactured via wrought and three different AM processes (EBAM, laser hot wire, selective laser melting) were tested in uniaxial tension and characterized via scanning electron microscopy to model and understand the plastic behavior and its dependence upon the materials state.

EBAM samples were produced using a raster scan strategy in a Sciaky system with an input heat source of ~8.5 kW, a travel speed of 12.7 mm/s and a "hatch spacing" between successive lines in the same layer of ~9 mm. The molten pool ranges from 10 to 16 mm and the layer thickness is ~3.3 mm. The depth of the molten pools exceeds 5 mm. After deposition three separate heat treatments were conducted: a low temperature stress-relief anneal (SR), a hot isostatic pressing (HIP) with temperatures in the α + β zone and a beta anneal (BA) with samples held shortly above the β transus temperature [4, 23].

Laser Hot Wire (LHW) samples were manufactured in a system at Oak Ridge National Laboratory (partner with Wolf Robotics, Lincoln Electric, Lockheed Martin), with an input heat source of ~ 3-6 kW, a raster strategy with travel speed of 2-15 mm/s, hot wire power of 50–500 W, melt pool area of 5-50mm^2, the adjacent hatches are ~ 3-10 mm. The LHW samples were analyzed in the as-deposited state, no heat-treatments were conducted.

The selective laser melting (SLM) of the Ti-6Al-4V was done using a Renishaw AM250 with the reduced build volume accessory and no build plate heating. The build atmosphere was high purity argon gas with an oxygen level at or below 100 ppm. The AM250 has a 200 W SPI Yb: fiber laser with a 1070 nm wavelength, and it was operated with

[1] In this paper, necking strain (i.e., uniform strain) is the strain at which the onset of necking occurs when a sample is loaded in tension.

a power modulated spotting pattern (i.e., pulsing) and an F-theta lens that provided a D4σ spot size of 70 µm. The build strategy that was used was a meander pattern with no border or contouring scans. During hatching the laser power was set to 180 W with an exposure time of 60 µs and a point distance of 69 µm. The distances between hatches was 90 µm, and the layer thickness 60 µm. No contouring pattern was used in any of the three AM processes.

Traditionally processed wrought Ti-6Al-4V in the beta annealed condition (and subsequently referred to as 'wrought') was subjected to the same heat-treatment procedure as that of the SLM material. The wrought and SLM Ti-6Al-4V were heat-treated using a Gleeble 3800 Thermal–Mechanical Physical Simulation System. The heat-treatments for these materials were selected through a design of experiments (DOE) to investigate the influence of four heat-treatment parameters (i.e., anneal time, cooling rate, stress relief temperature and stress relief time) on the resulting microstructure. Annealing times of 1 and 10 min were chosen to vary the amount of alpha phase dissolution high in the α + β phase field, while the annealing temperatures remained the same for all 28 heat treatments. The cooling rates span three orders of magnitude, and they were chosen to assess the well-known relationship that exists between α-lath thickness and cooling rate-i.e., α-lath thickness decreases with increasing cooling rate, or vice versa. For 18 heat treatments, the stress relief (SR) times and temperatures were chosen based on previous work with α + β-processed α/β Ti-based alloys to ensure near-equilibrium conditions [24]. Three different cooling rates ranging from 10 to 1,000 °C/min were chosen to represent slow, moderate and fast cooling rates relative to each other. Non-equilibrium conditions were chosen for six specimens, where the time and temperature were both at the minimum values for the stress relief step. For 4 of the 28 heat treatments, the final stress relief step was intentionally omitted following the non-equilibrium conditions.

Tensile coupons were machined and tested by Westmoreland Mechanical Testing and Research, Inc per ASTM E8 standards for EBAM and SLM samples at a strain rate of 0.005 mm/mm/min (8.3×10^{-5} s^{-1}), with a temporary stress reduction after yielding (to allow for the removal of extensometer used to precisely calculate the yield point and the elastic modulus) and a subsequent strain rate jump (SRJ) to values of either 0.05 mm/mm/min (8.3×10^{-4} s^{-1}) or 0.1 mm/mm/min ($1.6\times10-3$ s^{-1}) to reduce the overall testing time, as is customary. LHW samples were tensile tested at a nominal strain rate of ~ 0.002 mm/mm/min (3.3×10^{-5} s^{-1}), and the strain rate jump was not required in these samples, as the extensometer was removed during the test prior to fracture.[2] The effect of these testing protocols (the stress reduction as well as SRJ) on the crosshead data can be seen in Fig. 1; after yielding (910 MPa) the test was paused and relaxed (860 MPa) to remove the extensometer, and then the strain rate jump caused a very fast increase to 940 MPa.

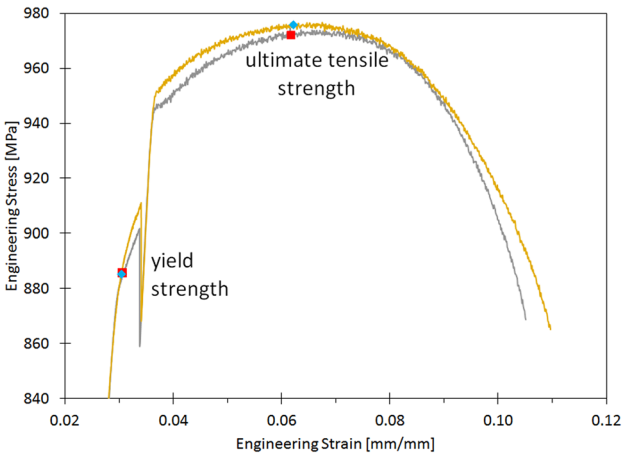

Fig. 1 Engineering plastic stress–strain curves of two SLM samples with similar yield strength and ultimate tensile strength values. This figure highlights the need to consider the true stress–strain curves, which is the emphasis of the paper. The discontinuity shown after the yield stress is because these tests started with an extensometer and a strain rate of 8.3×10^{-5} s^{-1}, after reaching the elastic limit the test was paused, the extensometer removed and the test continued at a higher strain rate (strain rate jump) of 8.3×10^{-4} s^{-1}

As shown in Fig. 1, only considering two discrete points (yield strength and ultimate tensile strength) is not sufficient to fully understand how the material behaves plastically. To understand the role of dislocations on the strength of the material beyond the elastic limit, and being able to predict the ultimate tensile strength, the KME model was selected. The first step was determining the k_1 and k_2 values that resulted in the best fit for each sample from the five databases. When plotting both variables, trend line equations (using mean squares) were obtained, separating strain rate jump (SRJ) values as different data series.

The process to construct full synthetic stress–strain curves was broken down into three primary components as shown in Fig. 2. The first step took composition and orientation information from a database as an input to set the slope of the elastic region (i.e., elastic modulus). In the second step, the previously developed yield strength equation was applied to calculate the strength. The KME model parameters were

[2] While the variation in experimental protocols may seem to be unusual, this paper aggregates work from multiple different programs with multiple different agencies and testing standards. The fact that the work results in models with such cross-standard interoperability is an important part of this paper.

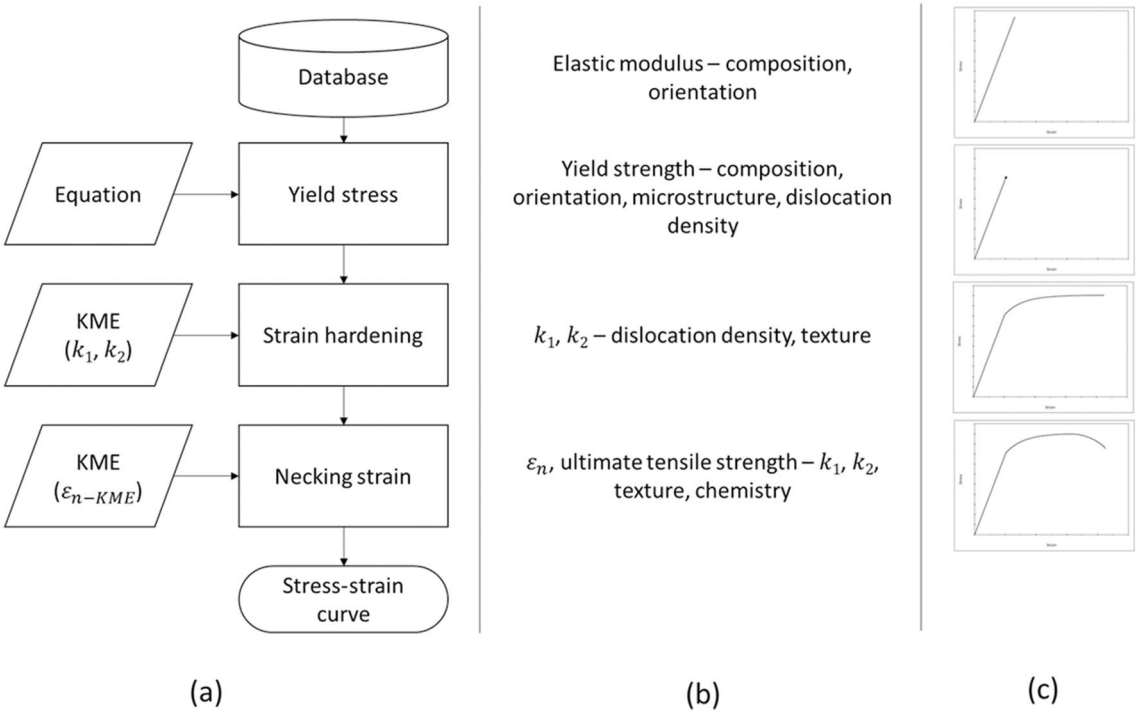

Fig. 2 Process used by the authors to obtain the entire true stress–true strain curve: **a** flowchart detailing the steps, **b** variables influencing each step, and **c** step-by-step progression of the full true stress–true strain curve construction

determined based on trends for each material condition, and thus, the average values were used for k_1 per dataset and condition (i.e., independent of whether a SRJ was included, and heat treatment) and each trend equation that relates k_1 and k_2. Ultimate tensile strength values were predicted for all samples and compared to the experimental ones. In total, 113 samples have been included in this work.

Results and Discussion

Backscattered scanning electron microscope micrographs illustrating microstructures as a result of their manufacturing process and heat treatment are shown in Fig. 3. The different manufacturing processes, as well as the variations in heat-treatments for the same process, result in notable differences in the morphologies and size of the microstructural features. For example, when comparing Fig. 3a, c, although both were produced via the EBAM process and have comparable average α-lath width, the different heat treatments result in morphological differences-i.e., colony in Fig. 3a and basketweave in Fig. 3c. However, when comparing Fig. 3b, c, a similar α-lath morphology is observed, but the average α-lath width of the HIP sample in Fig. 3b is slightly more than three times that of the stress relieved sample in Fig. 3c. Notably, the EBAM stress-relieved condition (Fig. 3c) and as-deposited LHW (Fig. 3d) result in basketweave microstructures with similar alpha lath widths, and as such one would expect the yield strength values to be similar considering the expression reported in [4]. SLM (Fig. 3e) produces mostly basketweave microstructures with almost double the alpha lath width as the stress-relieved EBAM (Fig. 3c). Finally, the wrought Ti-6Al-4V (Fig. 3f) has a basketweave microstructure with α-laths slightly thicker than the ones resulting from EBAM SR condition and the as-deposited LHW, which is indicative of the large variety of material states that can be achieved with different AM techniques and post-processing heat treatments. Unlike other Al, Fe, and Ni-base structural materials which often have coarse and brittle secondary phases (i.e., carbides, nitrides, and oxides), and which can have a substantial influence on strain accumulation, the microstructures observed for the alloy Ti-6Al-4V generally exhibits only the two course primary phases (i.e., the α and β phases), neither of which is brittle. Any deviation from this generality in Ti-6Al-4V will be in highly refined structures, such as very limited short range ordering in the alpha phase.

Randomly selected experimental stress–strain curves, one for each of the material conditions analyzed in this paper, are shown in Fig. 4. Notice the similar ultimate tensile strength value for datasets EBAM-SR, SLM and LHW (from 945 to 951 MPa) as well as the similarities between EBAM-BA and EBAM-HIP datasets (from 869 to 871 MPa), while the yield strength also follows the same behavior (825-866 MPa for

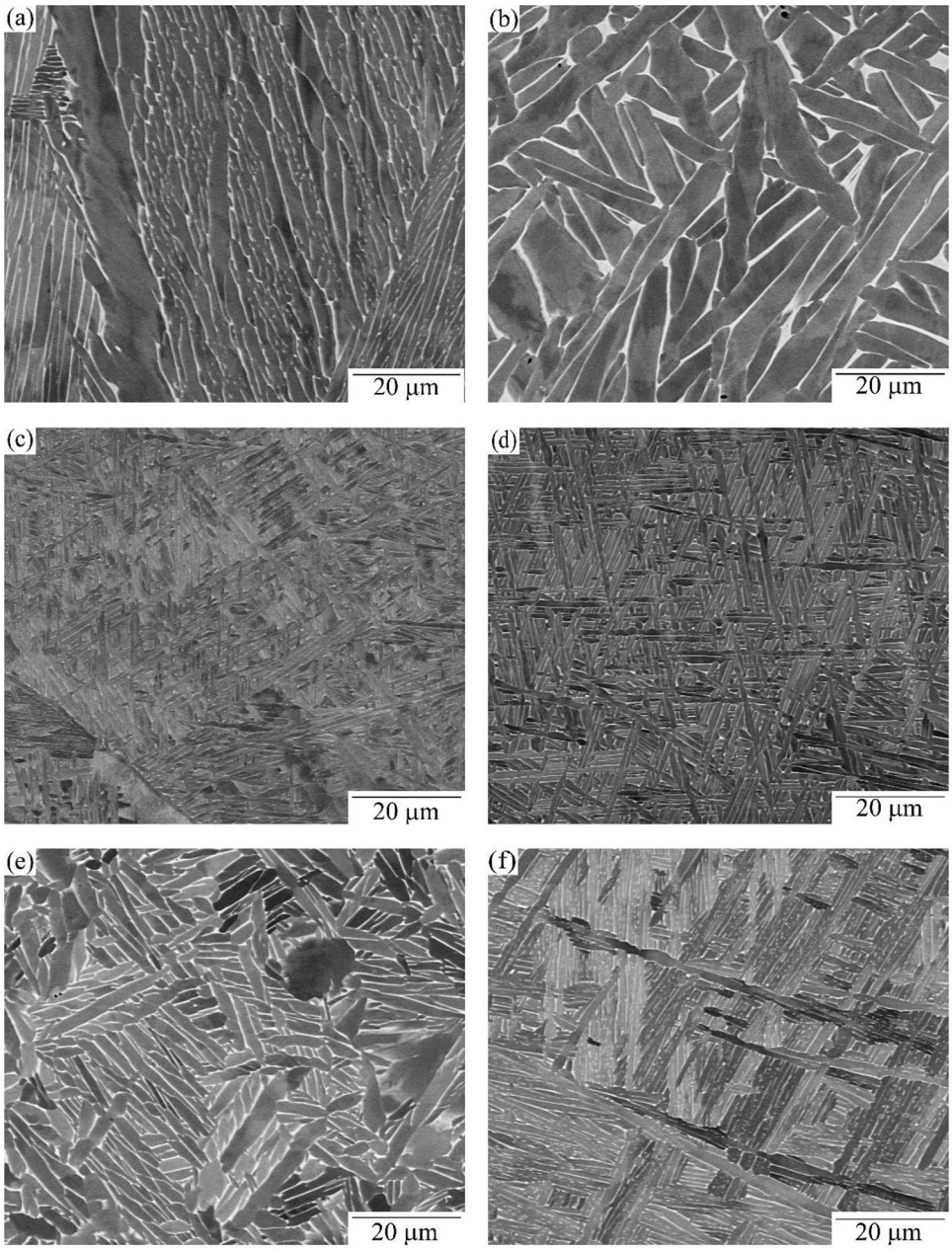

Fig. 3 Backscattered electron (BSE) SEM micrographs of Ti-6A-4V obtained by different manufacturing processes and heat treatments. The processes are: **a** EBAM-BA; **b** EBAM-HIP; **c** EBAM-SR; **d** LHW; **e** SLM; and **f** wrought. Note that all have been recorded at the same magnification to better illustrate the difference in scale/morphology. As is typical with Ti-6Al-4V BSE micrographs, the bright (white) phase is bcc beta and the dark (grays) phase is hcp alpha

EBAM-SR, SLM and LHW and 738-816 MPa for EBAM-BA and EBAM-HIP). This similarity in ultimate tensile strength of EBAM-BA and EBAM-HIP is not surprising, as comparable similarities in yield strength for these two conditions have previously been observed in [4]. While the beta anneal and HIP have very similar yield strength and ultimate tensile strength values, the path to reach ultimate tensile strength is different (as already noted in Fig. 1), and the different heat-treatment processes are the most likely contributors to the obvious difference in elongation.

Table 1 gives the average elastic modulus, yield strength, ultimate tensile strength and true ultimate tensile strength for each material condition. Additionally, the average yield strength and ultimate tensile strength is highest for the LHW material, which is notable due to the fact that LHW samples did not undergo any post build heat treatment and thus might exhibit the highest dislocation density / residual stress. As described in the methods section, there was no SRJ for the LHW samples. Although this paper reports elastic moduli determined via uniaxial tensile tests, more precise measurements of the elastic moduli can be obtained from further testing. Elastic moduli measured by nondestructive testing (NDT) methods are generally preferred. Examples of these NDT techniques include resonant ultrasound spectroscopy (RUS) and a special extension of spatially resolved acoustic spectroscopy (SRAS), both showing smaller standard

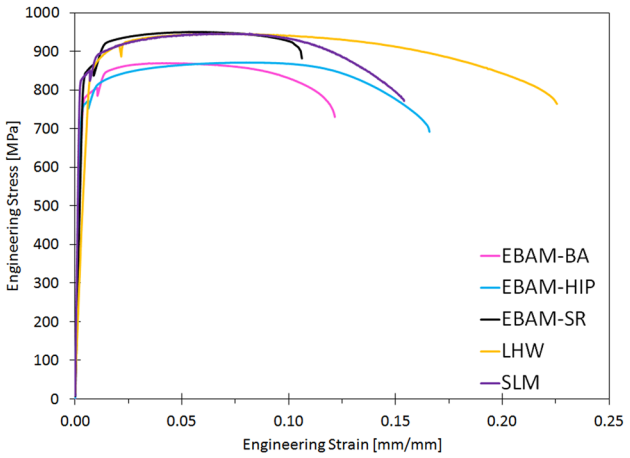

Fig. 4 Randomly selected engineering stress–strain curves of the three processes analyzed (with one of them with three different heat treatments). Note that these curves were created by combining data from extensometer (start of the test to immediately after yielding) and crosshead (from yielding to rupture). The strain rates when using extensometer are: 3.3×10^{-5} s^{-1} for LHW and 8.3×10^{-5} s^{-1} for EBAM and SLM. The strain rates were increased after the extensometers were removed (3×10^{-1} s^{-1} for EBAM and SLM)

deviations than traditional techniques, with SRAS also being able to assess large area (on the order of mm) orientation and texture [25, 26] in addition to the direct determination of the full elastic stiffness tensor (C_{ij}).

To compare the materials, an average value of k_1 and k_2 was determined for each AM material condition (i.e., EBAM-SR, EBAM-HIP, EBAM-BA, LHW and SLM, *see* Table 1) as well as wrought Ti-6Al-4V. A simple scatterplot (Fig. 5) illustrates a strong positive correlation between k_2 and k_1. Figure 5 shows that there is a *general* relationship between k_1 and k_2 (both wrought and AM, and with different heat treatments and manufacturing processes). This relationship can result in an approximate ultimate tensile strength value if the process and/or the heat treatment are known for a specific sample.

Of note is the fact that the SRJ condition appears to result in higher k_2 values, however, given the obvious positive correlation, k_1 appears to be higher as well. The higher k_1 value for the SRJ condition is an artifact of the strain rate sensitivity of the flow stress, as k_1 should be strain rate independent [27]. With all the material conditions except LHW experiencing loading at an initial strain rate, partial unloading, and reloading at a higher strain rate, a single flow stress value could not be used for the analysis of both the full and reloaded stress–strain curves. Therefore, it is important to note that, for the analysis of the reloaded stress–strain curves, a post-strain rate jump flow stress was determined, indirectly, through the addition of $\Delta\sigma$ to account for the increase in flow stress that accompanied the increase in strain rate.

The ultimate tensile strength was predicted for all materials, conditions, and test parameters using the KME model and the results are shown in Fig. 6. The results were predicted using average values for k_1 (*see* Table 1) and the expression for k_2 as a function of k_1. Almost all predicted values lie in the $\pm5\%$ range, with only one sample over the $+5\%$ line. This demonstrates the general applicability of the KME model for the prediction of ultimate tensile strength for Ti-6Al-4V manufactured by a variety of additive manufacturing and wrought processes.

Cumulative Probability Distributions

To analyze, more quantitatively, the confidence of these models, cumulative probability functions for the KME prediction of ultimate tensile strength were obtained (Figs. 7 and 8). Figure 7 considers all conditions and heat treatments as one set of data and compares experimental data (true UTS) to predictions considering parameters for the full curves (UTS_f) and after the strain rate jump (UTS_r). This figure also shows the root-mean-square error bounds (σ_{RMSE}), of both prediction models (full and SRJ) with the true ultimate tensile strength. UTS_f is closer to true UTS, with a σ_{RMSE} between them of 7.5 MPa (0.7% of the average true UTS), while the σ_{RMSE} between true UTS and UTS_r is 12.2 MPa (1.2%). The $\pm2\sigma_{\mathrm{RMSE}}$ represent approximately 95% confidence bounds, with almost all data points of the full curves between these bounds (dashed lines) with the exception of the points with values ~ 1200 MPa. In comparison, only 3 points from the SRJ dataset are outside their 95% bounds (continuous lines). Interestingly if instead of $\pm2\sigma_{\mathrm{RMSE}}$, $\pm3\sigma_{\mathrm{RMSE}}$ were plotted, all data from both datasets would be within these 99% confidence bounds.

Figure 8 shows the cumulative probability function separating each material condition. SLM and wrought data are very similar showing that heat treatments result in similar strength properties, regardless of a wrought or additive manufacturing process. The shift of EBAM compared to LHW can be explained by compositional differences, particularly of Al, that have been reported and that are related to the manufacturing process [4, 28, 29].

Application of Proposed Models

To construct a full stress–strain curve, or true stress—true strain in this case, the flowchart shown in Fig. 2a can be followed. The first step is to identify the elastic modulus, as this variable represents the slope for the elastic portion of the stress–strain curve. The values for the elastic modulus in AM Ti-6Al-4V can be obtained from databases and/or averages of tests such as uniaxial tensile tests, dynamic frequencies, nanoindentation, ultrasound, among others [30–32].

Table 1 Average values for elastic modulus, yield strength, ultimate tensile strength and KME model parameters (k_1 and k_2)

	Wrought	EBAM-BA	EBAM-HIP	EBAM-SR	LHW	SLM
Elastic modulus [GPa][a]	116.40	115.02	114.77	114.74	121.33	114.03
Yield strength [MPA]	861.94	783.24	762.00	873.34	901.18	859.27
Ultimate tensile strength [MPa]	961.79	879.71	869.68	960.96	981.15	958.74
True plastic ε_n	0.0457	0.0307	0.0650	0.0464	0.0634	0.0435
True ultimate tensile strength [MPa]	1067.14	956.38	974.09	1066.50	1051.44	1048.00
k_{1-f} [m^{-1}][b]	2.73×10^8	2.76×10^8	2.48×10^8	2.48×10^8	2.97×10^8	2.81×10^8
K_{2-f} [b]	41.50	39.91	32.86	37.92	53.83	41.68
Average true ultimate tensile strength f predicted [MPa][b]	1064.15 (error ± 3.7%)	982.73 (error ± 4.9%)	977.66 (error ± 2.5%)	1073.68 (error ± 2.5%)	1048.19 (error ± 3.5%)	1042.06 (error ± 3.4%)
True plastic $\varepsilon_{n-KME-f}$ [b]	0.0469	0.0524	0.0583	0.0483	0.0374	0.0496
Average stress jump after SRJ (Δσ) [MPa][b]	19.8	25.8	19.3	26.7	–	26.5
k_{1-SRJ} [m^{-1}][b]	3.05×10^8	3.37×10^8	2.75×10^8	2.78×10^8	–	2.90×10^8
K_{2-SRJ} [b]	55.57	76.82	44.00	59.75	–	56.23
Average true ultimate tensile strength SRJ predicted [MPa][b]	1059.16 (error ± 4.5%)	960.19 (error ± 2.1%)	972.15 (error ± 3.8%)	1061.44 (error ± 2.7%)	–	1043.18 (error ± 3.6%)
True plastic $\varepsilon_{n-KME-SRJ}$ [b]	0.0371	0.0286	0.0463	0.0330	–	0.0375

[a] E was obtained using an extensometer from the beginning of the test until right before yield strength

[b] f denotes full curve and SRJ after the strain rate jump. Wrought, EBAM-HIP, EBAM-SR and SLM started with a strain rate of 0.005 mm/mm/min and after removing the extensometer the strain rate was 0.05 mm/mm/min, while EBAM-BA started with 0.005 mm/mm/min and the rate increased to 0.1 mm/mm/min

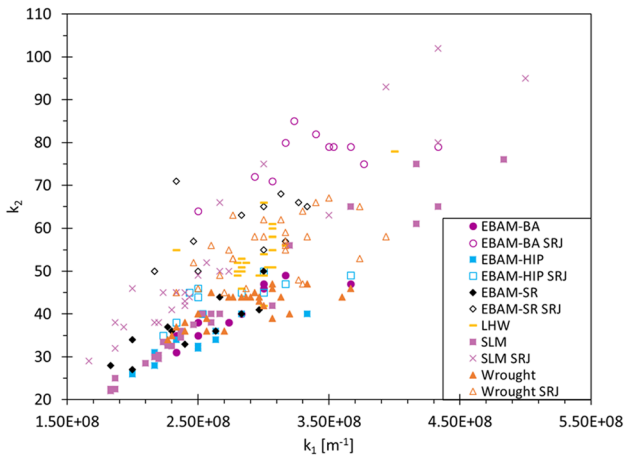

Fig. 5 KME model constants relationships for all material states tested ($k_1 - k_2$)

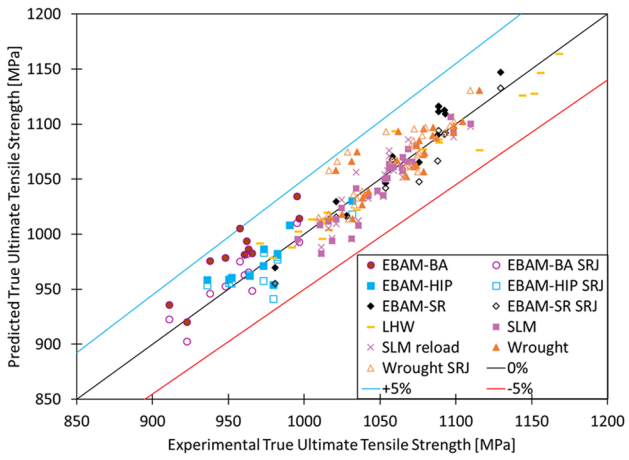

Fig. 6 Predicted vs experimental ultimate tensile strength for each material condition

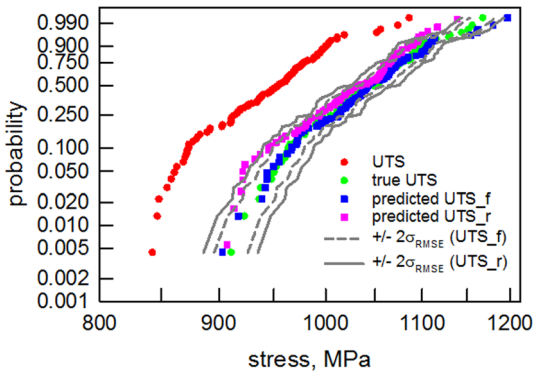

Fig. 7 Cumulative probability function of true ultimate tensile strength for all conditions. UTS_f represents full curves, UTS_r represents after strain rate jump. And RMSE the root-mean-square error

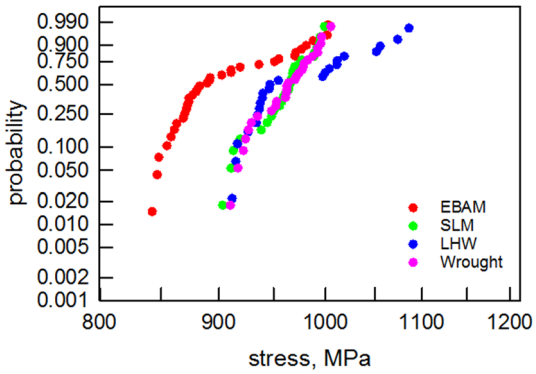

Fig. 8 Cumulative probability function of true ultimate tensile strength for all material conditions

The next critical data point to predict in the stress–strain curve is the yield stress. In the case of this work, this value was obtained using Eq. (1), considering microstructural and other characteristics of the samples. Once the yield strength is calculated, the KME model can be used to construct the plastic portion of the stress–strain curve. An average value for k_1 for the particular condition of the sample (manufacturing process, heat treatment) is used, as well as the already observed relationship between k_1 and k_2.

Figure 9 presents examples of comparisons of experimentally obtained curves (black lines) for four different manufacturing-heat-treatment conditions (EBAM-BA, EBAM-HIP, EBAM-SR and SLM) to the corresponding synthetic (i.e., predicted) curves (red dashed lines). To construct these synthetic curves, the elastic segment considered elastic modulus values from databases for each of these conditions, and the yield strength was calculated using Eq. 1. For the plastic segment, the KME equation (Eq. 3) was used, using the k_1 and k_2 average values for each respective material condition shown in Table 1. The same values for α, G, M and b were used for both yield strength prediction, as well as the KME equation, and the values can be found in the literature [4]. The predictions, as seen, follow the experimental ones very closely up to the ultimate tensile strength value, after which flow softening occurs, and which is not predicted by the KME model. Another slight deviation between the curves is observed when the experimental curves were paused to remove the extensometer, which is not, as expected, predicted by the model.

These results introduce the possibility for a new representation of stress–strain data. As shown previously, predicted stress–strain curves have been produced which match very closely to the experimentally observed stress–strain curves. With the modulus and yield strength, one can easily reconstruct the elastic region of any stress–strain curve. Additionally, given the correlation that exists between k_1 and k_2, one can apply the explicit solution given in Eq. 3 to reconstruct the plastic region of the stress–strain curve up until the ultimate tensile strength. This paper addresses strain rate jumps, which can add additional degrees of sophistication to this model. Therefore, in a prototypical KME model for a single strain rate test, if the manufacturing process of the Ti-6Al-4V sample is known, then only three material properties are necessary to generate an entire synthetic stress–strain curve through the ultimate tensile strength: elastic modulus, yield strength and k_1.

Future work could include the investigation of anisotropic effects, which are inherent to AM processes. However, while preliminary evidence suggests that orientation has an effect on both elastic and plastic properties, and likely strain accumulation, the discussion of the orientation of the columnar β-grains and their corollary features, such as the presence and spatial distribution of grain boundary alpha, with respect to the loading direction is outside the scope of this work.

Conclusions

The work presented here extends the development of phenomenological models by leveraging the Kocks–Mecking–Estrin (KME) model to predict the true stress, true strain behavior of a wide variety of additively manufactured Ti-6Al-4V. The salient conclusions of the paper are as follows:

- The KME model can be applied to accurately predict the stress–strain curve across all five material conditions with average values of relevant parameters k taken for each material condition.
- Important data related to different k's are presented for different strain rates. As the k's are dependent upon strain rate, this paper demonstrates that differences in testing conditions. Thus, the format of the equation itself does not change as a result of different testing preferences.

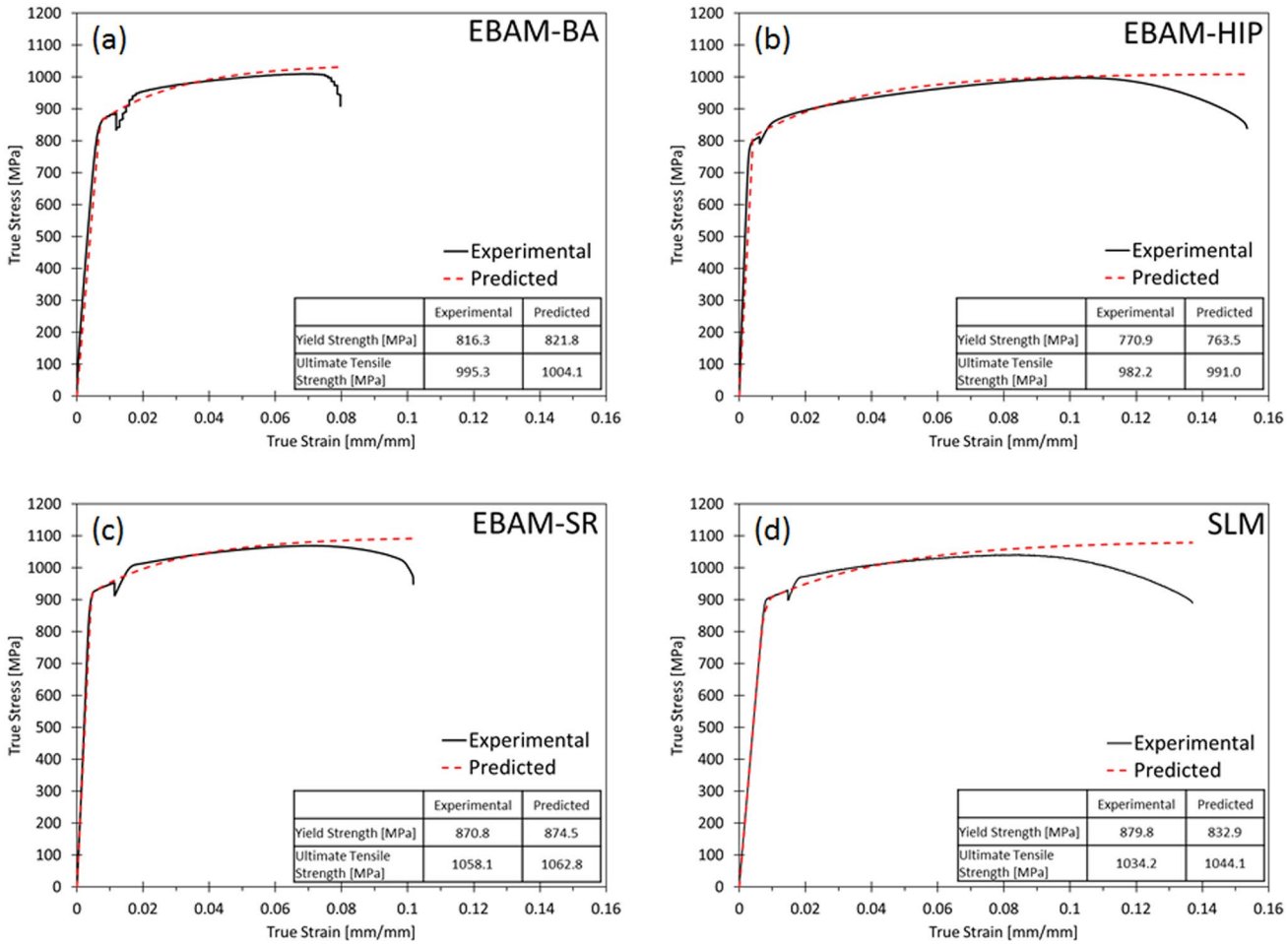

Fig. 9 Full synthetic true stress–true strain curves for randomly selected samples of the following manufacturing processes: **a** EBAM-beta anneal, **b** EBAM-HIP, **c** EBAM-stress relief, **d** selective laser melting. Note: the range of true stress and true strain on the ordinate and abscissa axes are kept constant to aid in visualizing the differences in mechanical behavior, and flexibility of the approach

- The KME model directly incorporates dislocation density, a rational strengthening mechanism that permits the correlation between strain accumulation and the corresponding strain hardening.
- This work represents the first time that full true stress, true strain curves have been predicted using such phenomenological tools for AM-Ti-6Al-4V using both a previously reported equation for yield strength and the addition of the KME model to go from yield strength to ultimate tensile strength.
- The method outlined in this work for the prediction of the ultimate tensile strength is within 5% across all five material conditions, and thus, this method has been demonstrated to be applicable to a wide range of traditional and advanced manufacturing processes, including post deposition heat treatments for Ti-6Al-4V.
- The workflow outlined in this paper shows that a fully synthetic stress–strain curve can be constructed from average values. Average values for a specific process/heat-treatment type are adequate for predicting the ultimate tensile strength of all samples that fall within that predefined category.

Acknowledgements This work represents the aggregation of data from four research programs. The EBAM materials were produced, heat-treated, and tested under the DARPA contract HR0011-12-C-0035 ("An Open Manufacturing Environment for Titanium Fabrication"). Subsequent investigations into the fundamental mechanisms of ultimate tensile strength were supported in part by Boeing. The LHW additively manufactured materials were produced and tested, and investigations into the fundamental mechanisms of ultimate tensile strength were supported in part under the ONR contract N00014-18-C-1026 ("Robotic Laser Additive Manufacturing System with Comprehensive Quality Assurance Framework"). The SLM additively manufactured materials were produced and tested, and investigations into the fundamental mechanisms of ultimate tensile strength were supported in part under a contract from Honeywell Federal Manufacturing and Technologies LLC, contract number 705164 ("Beta Stabilized Titanium for SLM"), and thus under Honeywell FM&T's Prime Contract Number DE-NA0002839 with the U.S. Department of Energy. The

views, opinions and/or findings expressed are those of the author and should not be interpreted as representing the official views or policies of the Department of Defense or the U.S. Government. The authors would like to thank the technical points of contacts from the different research programs for their input and technical conversations, including: Andrew H. Baker and, now retired, David M. Bowden at The Boeing Company; Benjamin Brown, Benjamin Sikora and Camille Baker from Kansas City National Security Campus; and Glynn P. Adams and Edward A. Pierson from Lockheed Martin.

Declarations

Conflict of interest On behalf of all authors, the corresponding author states that there is no conflict of interest.

References

1. Buynak CF, Blackshire J, Lindgren EA, Jata KV (2008) Challenges and opportunities in NDE, ISHM and material state awareness for aircraft structures: US air force perspective. In: AIP conference proceedings, 1789–1801. https://doi.org/10.1063/1.2902653
2. Jacobs LJ (2014) Nonlinear ultrasonics for material state awareness. In: AIP conference proceedings, 13–20. https://doi.org/10.1063/1.4864797
3. Aldrin JC, Lindgren EA (2017) The need and approach for characterization-U.S. air force perspectives on materials state awareness. Science. https://doi.org/10.1063/1.5031501
4. Hayes BJ, Martin BW, Welk B et al (2017) Predicting tensile properties of Ti-6Al-4V produced via directed energy deposition. Acta Mater 133:120–133. https://doi.org/10.1016/j.actamat.2017.05.025
5. Liu S, Shin YC (2019) Additive manufacturing of Ti6Al4V alloy: a review. Mater Des 164:107552. https://doi.org/10.1016/j.matdes.2018.107552
6. Ludwik P (1909) Elemente der Technologischen Mechanik. Springer, Berlin
7. Hollomon JH (1945) Tensile deformation. Trans Metall Soc AIME 162:268–290
8. Voce E (1948) The relationship between stress and strain for homogeneous deformation. J Inst Met 74:537–562
9. Swift HW (1952) Plastic instability under plane stress. J Mech Phys Solids 1:1–18. https://doi.org/10.1016/0022-5096(52)90002-1
10. Ghamarian I, Samimi P, Dixit V, Collins PC (2015) A constitutive equation relating composition and microstructure to properties in Ti-6Al-4V: as derived using a novel integrated computational approach. Metall Mater Trans A 46:5021–5037. https://doi.org/10.1007/s11661-015-3072-4
11. Ghamarian I, Hayes B, Samimi P et al (2016) Developing a phenomenological equation to predict yield strength from composition and microstructure in β processed Ti-6Al-4V. Mater Sci Eng A 660:172–180. https://doi.org/10.1016/j.msea.2016.02.052
12. Littlewood PD, Britton TB, Wilkinson AJ (2011) Geometrically necessary dislocation density distributions in Ti-6Al-4V deformed in tension. Acta Mater 59:6489–6500. https://doi.org/10.1016/j.actamat.2011.07.016
13. Babu B, Lindgren LE (2013) Dislocation density based model for plastic deformation and globularization of Ti-6Al-4V. Int J Plast 50:94–108. https://doi.org/10.1016/j.ijplas.2013.04.003
14. Gorsse S, Hutchinson C, Gouné M, Banerjee R (2017) Additive manufacturing of metals: a brief review of the characteristic microstructures and properties of steels, Ti-6Al-4V and high-entropy alloys. Sci Technol Adv Mater 18:584–610. https://doi.org/10.1080/14686996.2017.1361305
15. Sun H, Liang Y, Li G et al (2021) Dislocation hardening and phase transformation-induced high ductility in Ti-6Al-4V with a heterogeneous martensitic microstructure under tensile load. J Alloys Compd 868:159155. https://doi.org/10.1016/j.jallcom.2021.159155
16. Mecking H, Kocks UF (1981) Kinetics of flow and strain-hardening. Acta Metall 29:1865–1875. https://doi.org/10.1016/0001-6160(81)90112-7
17. Kocks UF, Mecking H (2003) Physics and phenomenology of strain hardening: The FCC case. Prog Mater Sci 48:171–273
18. Estrin Y, Molotnikov A, Davies CHJ, Lapovok R (2008) Strain gradient plasticity modelling of high-pressure torsion. J Mech Phys Solids 56:1186–1202. https://doi.org/10.1016/j.jmps.2007.10.004
19. Ahn DH, Kim HS, Estrin Y (2012) A semi-phenomenological constitutive model for hcp materials as exemplified by alpha titanium. Scr Mater 67:121–124. https://doi.org/10.1016/j.scriptamat.2012.03.037
20. Yasnikov IS, Vinogradov A, Estrin Y (2014) Revisiting the Considère criterion from the viewpoint of dislocation theory fundamentals. Scr Mater 76:37–40. https://doi.org/10.1016/j.scriptamat.2013.12.009
21. Vinogradov A, Yasnikov IS, Estrin Y (2015) Irreversible thermodynamics approach to plasticity: dislocation density based constitutive modelling. Mater Sci Technol (UK) 31:1664–1672. https://doi.org/10.1179/1743284715Y.0000000069
22. Yasnikov IS, Estrin Y, Vinogradov A (2017) What governs ductility of ultrafine-grained metals? A microstructure based approach to necking instability. Acta Mater 141:18–28. https://doi.org/10.1016/j.actamat.2017.08.069
23. Baker AH, Collins PC, Williams JC (2017) New nomenclatures for heat treatments of additively manufactured titanium alloys. JOM 69:1221–1227. https://doi.org/10.1007/s11837-017-2358-y
24. Collins PC, Welk B, Searles T et al (2009) Development of methods for the quantification of microstructural features in α + β-processed α/β titanium alloys. Mater Sci Eng A 508:174–182. https://doi.org/10.1016/j.msea.2008.12.038
25. Gorsse S, Miracle DB (2003) Mechanical properties of Ti-6Al-4V/TiB composites with randomly oriented and aligned TiB reinforcements. Acta Mater 51:2427–2442. https://doi.org/10.1016/S1359-6454(02)00510-4
26. Dryburgh P, Li W, Pieris D et al (2022) Measurement of the single crystal elasticity matrix of polycrystalline materials. Acta Mater. https://doi.org/10.1016/j.actamat.2021.117551
27. Estrin Y, Mecking H (1984) A unified phenomenological description of work hardening and creep based on one-parameter models.

Acta Metall 32:57–70. https://doi.org/10.1016/0001-6160(84)90202-5
28. Keist JS, Nayir S, Palmer TA (2020) Impact of hot isostatic pressing on the mechanical and microstructural properties of additively manufactured Ti–6Al–4V fabricated using directed energy deposition. Mater Sci Eng A. https://doi.org/10.1016/j.msea.2020.139454
29. Brice CA, Tayon WA, Newman JA et al (2018) Effect of compositional changes on microstructure in additively manufactured aluminum alloy 2139. Mater Charact 143:50–58. https://doi.org/10.1016/j.matchar.2018.04.002
30. Ide JM (1935) Some dynamic methods for determination of Young's modulus. Rev Sci Instrum 6:296–298. https://doi.org/10.1063/1.1751876
31. Majumdar P, Singh SB, Chakraborty M (2008) Elastic modulus of biomedical titanium alloys by nano-indentation and ultrasonic techniques-a comparative study. Mater Sci Eng A 489:419–425. https://doi.org/10.1016/j.msea.2007.12.029
32. Wang P, Todai M, Nakano T (2019) Beta titanium single crystal with bone-like elastic modulus and large crystallographic elastic anisotropy. J Alloys Compd 782:667–671. https://doi.org/10.1016/j.jallcom.2018.12.236